



# Preparation and characterization of metals supported on nanostructured TiO<sub>2</sub> hollow spheres for production of hydrogen via photocatalytic reforming of glycerol



Tumelo W.P. Seadira<sup>a,\*</sup>, Gullapelli Sadanandam<sup>a</sup>, Thabang Ntho<sup>b</sup>, Cornelius M. Masuku<sup>a,\*</sup>, Michael S. Scurrell<sup>a,\*</sup>

<sup>a</sup> Department of Civil and Chemical Engineering, University of South Africa, Private Bag X6, FL, 1710, South Africa

<sup>b</sup> Advanced Materials Division, Mintek, Randburg, South Africa

## ARTICLE INFO

### Keywords:

Photocatalysis  
Biomass  
Glycerol  
Titania hollow spheres  
Renewable hydrogen

## ABSTRACT

Nanostructured TiO<sub>2</sub> hollow spheres (THS) were prepared via a simple hydrothermal method with titanium butoxide, ethanol, urea, and ammonium sulphate. The effects of Ti/ethanol, and reflux temperature on the morphological properties of the nanostructured THS were investigated. An impregnation method was subsequently employed to load metals such as Cu, Co, Cr, Ag, and Ni on the optimized THS, followed by calcination in H<sub>2</sub>/N<sub>2</sub> at 450 °C for 4 h. The morphological properties of the prepared samples were characterized by Brunauer-Emmett-Teller (BET), X-ray diffraction (XRD), scanning electron microscopy (SEM), transmission electron microscopy (TEM), and ultraviolet-visible spectroscopy (UV/vis). The SEM and TEM pictures showed that the Ti/ethanol ratio of 1:10 resulted in the formation of uniform hollow spheres. The XRD spectra revealed that phase transformation took place as the reflux temperature was increased, with pure anatase TiO<sub>2</sub> hollow spheres being formed at 200 °C. The BET surface areas of the calcined photocatalysts were in the range of 80.6–116 m<sup>2</sup>/g<sup>-1</sup>. The UV/vis spectra of the photocatalysts showed that loading of transition metals reduced the band gap of the THS. The activities of the prepared catalysts were tested for hydrogen production via photocatalytic reforming of glycerol under solar irradiation. The improved hydrogen evolution from photocatalytic reforming of glycerol was attributed to: the high surface area which enhanced the adsorption of glycerol onto the surface of photocatalysts; high crystallinity and the reduced band gap which improved the solar light harvesting; the hollow chamber within the TiO<sub>2</sub> spheres which produced multiple reflection of the light harvested, thus producing efficient electron/hole pair formation; and the detailed composition of the solids retarded the electron/hole recombination by trapping the electrons generated during the photo excitation of the photocatalysts, and thereby promoted their activity.

## 1. Introduction

The increase in population has raised alarms regarding energy demands, and most of the world's energy is produced from non-renewable energy sources such as fossil fuels. However, it has been predicted that these fossil fuels will be depleted in the near future due to the increased rate of their exploitation. Therefore, due to the inevitable depletion of the fossil fuels, and the global climate change which is caused by the combustion of these fuels, research has been directed towards finding alternative energy sources which are renewable and environmentally friendly [1,2]. Hydrogen is recognised as an alternative ecologically friendly energy vector due to its high combustion energy of 120 MJ/kg, which is higher than any other source of energy; and also because of its

zero percentage carbon emissions [3,4]. Currently, most of the world's sustainable hydrogen is being produced from commercial processes such as pyrolysis, steam reforming, and steam gasification using renewable biomass and water as sources of hydrogen [5–7]. These commercial processes however, require large amounts of energy which makes them costly, and they tend to leave a large carbon footprint on the environment. Photocatalytic production of hydrogen from renewable biomass such as glycerol, over semiconductor photocatalysts, under solar irradiation is a potential alternative process which is environmentally friendly, not costly, and easy to set up and operate [8–11]. Titanium dioxide, TiO<sub>2</sub> is widely employed as catalyst since it is low cost, non-toxic, biologically and chemically stable, and it is resistant to photocorrosion. Unfortunately, it has been reported

\* Corresponding authors.

E-mail addresses: [scurrm@unisa.ac.za](mailto:scurrm@unisa.ac.za), [mike.scurrellunisa@gmail.com](mailto:mike.scurrellunisa@gmail.com) (M.S. Scurrell).

previously that  $\text{TiO}_2$  showed poor activity during water splitting under solar irradiation because of its wide band gap of 390 nm [12]. This large band gap limits the activity of  $\text{TiO}_2$  to ultraviolet (UV) irradiation, which only makes up < 6% of the solar spectrum, whilst visible light makes up ~40% of the solar spectrum. Furthermore, the low activity of the pure  $\text{TiO}_2$  during the hydrogen production was attributed to the accelerated recombination of photogenerated electron/hole pairs and the reverse reaction of the intermediates produced [13]. Gholipour et al., [14] reported that incorporation of metals or metal oxides with  $\text{TiO}_2$  as co-catalysts can enhance the activity and retard the electron/hole recombination during photocatalytic water splitting.

Over the past few decades,  $\text{TiO}_2$  materials with varying nanostructures and morphologies have been successfully prepared, and hollow spheres of nanostructured  $\text{TiO}_2$  have received a lot of attention because of their potential application as photocatalysts/supports; their excellent photocatalytic ability is attributed to the multiple light reflection which occurs inside their hollow chambers, and their ease of separation from the reaction mixture [15–17]. The hollow spheres of  $\text{TiO}_2$  have been prepared using template-assisted sacrificial methods; however, the removal of these templates is a very complex and energy consuming process [18]. Recently, these hollow spheres  $\text{TiO}_2$  have been successfully prepared using template-free methods, which makes ease of handling and upscaling practical.

[19] Wang et al., [20] successfully prepared  $\text{TiO}_2$  hollow spheres (THS) with enhanced photocatalytic activity of hydrogen production via a facile, template-free hydrothermal method. In this paper, we report on the successful preparation of THS via a simple one-pot hydrothermal method; and the loading of transition metals onto the surface of the THS by incipient wet impregnation. The activities of the prepared catalysts for the photocatalytic production of hydrogen from glycerol reforming have been assessed. This study gives new insights into the incorporation of transition metals into the surface of the THS in order to enhance the photocatalytic activity for improved hydrogen evolution.

## 2. Experimental

### 2.1. Preparation of M/THS photocatalysts

All the reagents used in this study were of analytical grade and were used as received. The nanostructured THS were successfully prepared by a simple one-pot hydrothermal method. First, ammonium sulphate (12 g) and urea (5 g) were dissolved in desired mass of absolute ethanol in a reaction flask, under vigorous stirring for 45 min. Titanium butoxide of desired mass was added dropwise to the resulting mixture under vigorous stirring, and the whole subsequently aged overnight. The resulting precipitates-transparent liquid mixture was then refluxed at desired temperatures for 5 h, and subsequently allowed to cool naturally to room temperature. The precipitates were filtered, and then washed three times with high purity distilled water, followed by washing five times with absolute ethanol. The resulting powders were oven-dried overnight at 120 °C. The Ti/ethanol ratio and reflux temperature were varied in order to investigate their effect on the formation of THS. The incipient wetness impregnation method was used to load transition metals, Ni, Cu, Co, Ag, or Cr onto the surface of the THS; and the impregnated samples were calcined at 450 °C in flowing 20%  $\text{H}_2/\text{N}_2$  for 5 h. The prepared samples were denoted as: plain THS, THS@450C, Ni/THS, Cu/THS, Co/THS, Ag/THS, and Cr/THS.

### 2.2. Structural characterization

The crystal phase structure of the prepared THS and M/THS photocatalysts were analyzed by X-ray power diffraction (Bruker AXS D8 Advance). The XRD patterns were recorded at room temperature with scanning speed of  $2^\circ \text{ min}^{-1}$  using  $\text{Co K}_\alpha$  radiation ( $\lambda = 1.8 \text{ nm}$ ) from a 40 kV X-ray source and diffracted beam monochromator, operated at 35 mA. Scanning electron micrograph (SEM) images were obtained

using an FEI NOVA NANOSEM 200. The samples were deposited on a sample holder with a piece of adhesive tape in order to make them conductive, and subsequently inserted in the SEM. Transmission electron microscopy (TEM) images were recorded using the LEO 912 OMEGA TEM, operating at 120 kV, equipped with Proscan CCD camera for digital image acquisition. The images were analyzed using the Soft Image System (SIS) software. The Autosorb-I (Quantachrome) equipment was used to obtain the Brunauer-Emmett-Teller (BET) surface areas and porosity properties of the photocatalysts by  $\text{N}_2$  adsorption at  $-196^\circ\text{C}$ . The GBC UV-vis Cintra 10e spectrophotometer was employed to record the UV-vis diffuse reflectance spectra (DRS) at room temperature in the range of 300–700 nm. The photoluminescence (PL) emission and excitation (PLE) properties of the prepared materials were probed using an Edinburgh Instrument FS920 photoluminescence spectrometer with an excitation wavelength of 350–380 nm, using Xe light as the light excitation source. The widths of the emission slit and excitation slit were both 10 nm.

### 2.3. Photocatalytic activity

The photocatalytic hydrogen production tests were performed in a 150 mL quartz reactor under solar irradiation. First, 50 mL of solution containing 5% (v/v) glycerol was prepared with high purity distilled water, and 100 mg prepared samples were used as the photocatalyst. The glycerol solution, together with the prepared photocatalyst was added into the quartz reactor which was sealed with a silicone rubber septum. Prior to solar irradiation, the slurry in the reactor was evacuated for 30 min and bubbled with helium for 50 min in order to completely remove the dissolved oxygen and to ensure that the reactor was operating in an anaerobic condition. The catalyst was kept in suspension by continuous magnetic stirring during the entire period of the experiment. The analysis of  $\text{H}_2$  evolved was conducted every 1 h for 4 h by extracting 0.5 mL of the gas sample from the reactor and subsequently injecting it into the gas chromatograph (Shimadzu GC-2010) using He as a carrier gas.

## 3. Results and discussion

### 3.1. SEM analysis

**Fig. 1** shows the SEM images of the plain THS prepared from different titania/ethanol ratios. The overall morphology shown in high-magnification SEM images [**Fig. 1(a)-(b)**] revealed that the samples consisted of uniform spherical particles with diameters in ranges 60–125 nm and 86–115 nm, respectively. Furthermore, a rough surface of the spheres observed from **Fig. 1(a)-(b)** indicated that the aggregation of numerous spherical and irregular shaped  $\text{TiO}_2$  nanoparticles of 60–125 nm and 86–115 nm, respectively, took place via self-assembly to form hollow spheres with diameter of 0.6–1.25  $\mu\text{m}$ . Moreover, it was observed that a higher concentration of the titania precursor [**Fig. 1(a)**] lead to formation of larger spherical particles with rougher surfaces due to a higher growth rate, although the particles appeared to have aggregated into clusters. When the titania/ethanol ratio was increased to 1:10, uniform spherical particles were achieved. However, no uniform spherical particles were observed from **Fig. 1 (c)**; which suggests that the ratio of titania-solvent plays an important role in the formation of hollow spheres [20,21]. Therefore, the optimum titania/ethanol ratio was found to be 1:10.

**Fig. 2** shows the SEM images of prepared samples using the titania/ethanol optimum ratio and which underwent hydrothermal processes at different temperatures for 5 h. It is observed that the prepared samples retained their spherical structure, even after undergoing hydrothermal treatment at 200 °C, but the particle size increased along with some aggregation. However, **Fig. 2(a)** shows that the hydrothermally treated aggregates at 80 °C appear to be loosely packed, but as the hydrothermal temperature is increased, the aggregates become compacted.

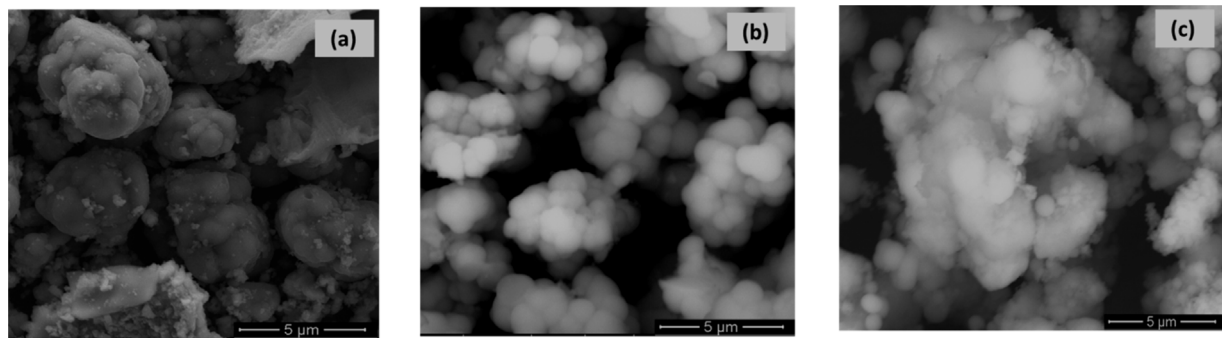


Fig. 1. SEM images of THS prepared with varying titania/ethanol ratio, (a) 1:5, (b) 1:10, (c) 1:15.

The TEM and XRD analysis were also applied to provide insights into the structure, particularly validating that the spheres consisted of hollow chambers (Fig. 3), and to study the effect of hydrothermal temperature on the structure and the crystalline properties of the prepared samples.

### 3.2. TEM analysis

The TEM was used to investigate the internal structure of the prepared samples. Fig. 4 shows the internal structures of the titania samples prepared from varying Ti/ethanol ratios. It is seen that the ratio of the Ti/ethanol plays a crucial role during the formation of titania hollow spheres. It is clearly seen that when the ratio of 1:5 (Ti/ethanol) was used, hollow triangle-like particles of about 0.9 μm were formed with a shell thickness of about 200 nm [Fig. 4(a)]. The hollow chamber of the triangle-like particle was indicated by strong contrast between the dark centre and light edges. The hollow spherical particles were successfully prepared using the Ti/ethanol ratio of 1:10, with the diameter of the hollow chamber ranging between 0.3–1.1 μm and the shell thickness of 135–300 nm [Fig. 4(b)]. The TEM analysis also confirmed the SEM analysis, that irregular shaped titania particles were formed when a Ti/ethanol ratio of 1:15 was used. Fig. 5 shows the TEM pictures of titania hollow refluxed at various temperatures. It is observed that the reflux temperature had no effect on the morphology of the samples, as is clearly seen from the images, in that the samples retained their spherical shape. However, the samples increased in size due to further aggregation of the titania nanoparticles. The diameter of the hollow chambers was in the range 0.8–1.4 μm, and the shell thickness was 175–286 nm. Similar TEM images of titania hollow spheres were reported by Liu et al. [22]. Furthermore, it was observed that the THS particles were connected to each other to form uniform multimers due to the existence of the Ti-OH groups on the surface of the spheres [23].

The formation of  $\text{TiO}_2$  hollow spheres can be explained as follows: Precipitation of titania in ethanol allows for controlled synthesis of the desired hollow structures due to the slow rates of the process because of

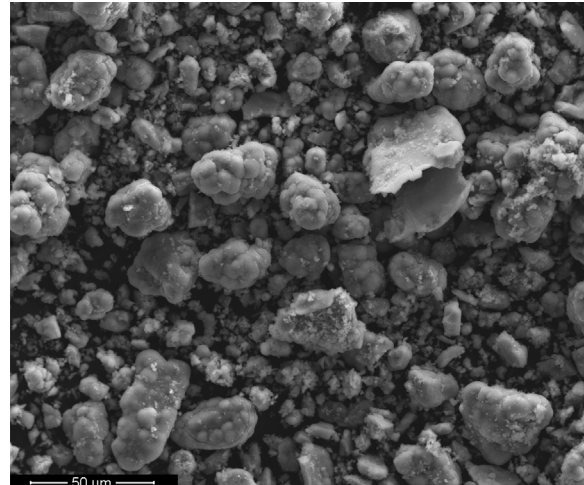


Fig. 3. SEM image of the titania, showing the hollow sphere nature of the particles.

the limited water available. The precipitated titania is then promoted by the  $\text{OH}^-$  produced together with  $\text{CO}_2$  bubbles during the decomposition of urea; and the resulting titania precipitate in turn aggregates and assembles around the  $\text{CO}_2$ -liquid interface to form  $\text{TiO}_2$  hollow spheres [21]. Furthermore, the assembling of titania precipitates around the  $\text{CO}_2$ -liquid is achieved due to the zeta potential modification of the titania precipitate by ammonium sulphate, which acts as an electrolyte [24]. This two-staged process is commonly known as the Ostwald ripening process, which has a tolerance for high reaction temperatures in the range of 150–180 °C whereby uniform hollow spheres can be obtained [25].

### 3.3. XRD analysis

Fig. 6 (left) shows the XRD patterns of the samples prepared with

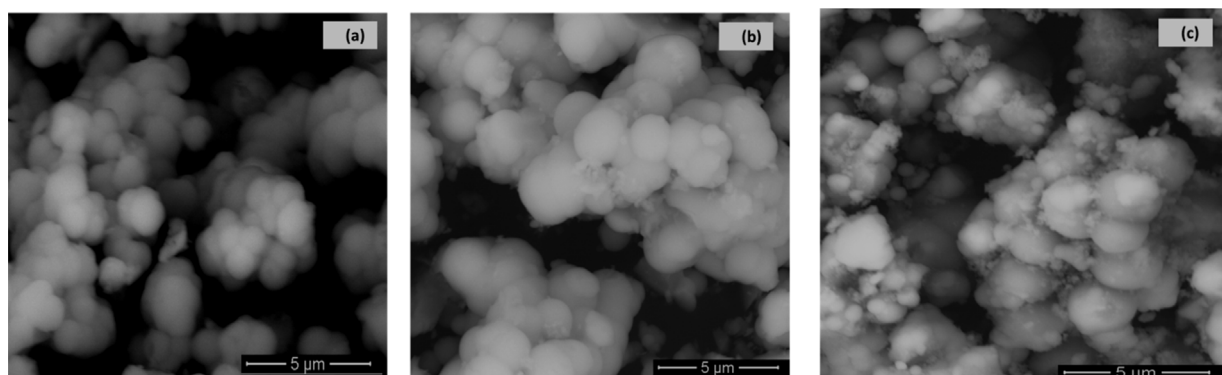


Fig. 2. SEM images of THS prepared from varying hydrothermal treatment temperature, (a) 80 °C, (b) 160 °C, (c) 200 °C.

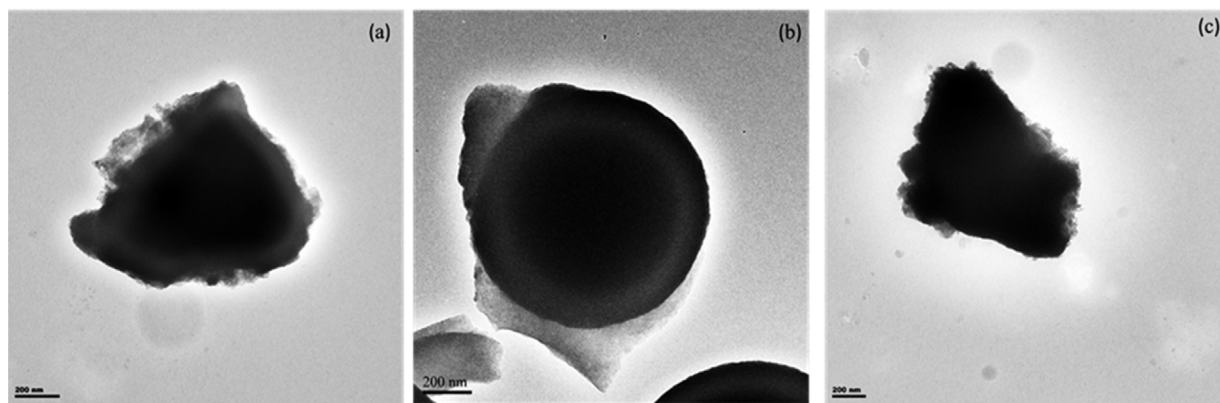


Fig. 4. TEM Images of THS prepared from varying Ti/ethanol ratio: (a) 1:5, (b) 1:10, (c) 1:15.

the optimum titania/ethanol ratio of 10, and subjected to hydrothermal treatment at different temperatures. From the XRD patterns, it was observed that the hydrothermal treatment temperature plays a crucial role on the phase transformation process of the prepared samples. The crystal phase transformation from amorphous to anatase was achieved with the use of increasing temperatures from 80 to 200 °C. The presence of diffraction peaks of the plain sample hydrothermally treated at 200 °C, were determined as  $2\theta = 28.6, 44.3, 55, 66$ , and  $74^\circ = \text{t}$  which correspond to the (101), (004), (200), (211), and (204) crystal planes of anatase  $\text{TiO}_2$ , respectively.

The average crystallite size of the plain sample was determined using the Scherrer equation ( $D = K \lambda/\beta \cos \theta$ ) based on the main anatase diffraction (101) peak; where  $D$  is the crystallite size,  $\lambda$  is the X-ray wavelength (1.789),  $\beta$  is the full-width at half maximum (FWHM) of the diffraction peak (radian),  $K$  is a coefficient (1), and  $\theta$  is the diffraction angle at the maximum peak; the values of  $\theta$  and  $\beta$  were taken from the main  $\text{TiO}_2$  diffraction line [26]. The average crystallite size was estimated to be 3.9 nm, which suggested that the anatase  $\text{TiO}_2$  particles are composed of nanocrystal subunits [27]. Therefore, the plain THS sample hydrothermally treated at 200 °C was considered as the optimized material, and was employed for further studies. The optimized THS sample was impregnated with 2 wt% of various metals such as Cu, Ag, Co, Cr, and Ni; and calcined in  $\text{H}_2/\text{N}_2$  for 3 h.

Fig. 6 (right) shows the XRD patterns of the optimized THS impregnated with different metals. It is observed from the XRD patterns that all THS samples are made up of anatase as the dominant crystalline phase, with diffraction peaks determined to be 28.6, 44.8, 55, 66, 74, 85, and 90° by employing the phase representation method (search/match from the EVA library database), which corresponds to the (101), (004), (200), (211), (204), (220), and (215) planes [20]. These sharp diffraction peaks indicated the well crystallized nature of the THS which underwent calcination. No obvious peaks of any of the metals

loaded were observed, which suggested that the metals were well dispersed on the surface of  $\text{TiO}_2$  samples [28,29]. Furthermore, the shape and the intensity of the peaks remained relatively unchanged for all the metal-impregnated THS samples, which inferred that the metals impregnation resulted in insignificant changes in the phase structure of the THS. The crystallite sizes of calcined samples were also determined by the Scherrer equation, and they are listed in Table 1. The crystal growth of the anatase crystallites increased with calcination temperature, but however decreased due to the metal loading. This could be attributed to the restrained grain growth in the presence of the impregnated metals, which in turn led to a smaller crystallite size at a given mass composition [30,31].

#### 3.4. BET

Fig. 6 shows the  $\text{N}_2$  adsorption/desorption isotherms and pore size distribution of the plain  $\text{TiO}_2$  samples as well as the metal-impregnated THS samples. The  $\text{N}_2$  adsorption/desorption isotherms of plain THS are indicative of type IV behaviour, according to the IUPAC classification and the typical H4 hysteresis loop. The capillary condensation occurs at relative pressures ( $P/P_0$ ) of 0.0–0.95, indicating a uniform mesoporous diameter distribution. It was also determined that the  $\text{N}_2$  adsorption/desorption plots of all calcined THS samples exhibited type IV behaviour, characteristic of mesoporous materials. The hysteresis loops for all metal-impregnated THS samples were ascribed to H2, and the hysteresis loop of the plain THS sample was H3, which is associated with narrow slit-like pores [32]. The pore size distributions plots (Fig. 7) of all samples exhibited a narrow distribution which indicated that the pores size was homogeneous. The BET surface areas and the average pore sizes calculated using the BJH equation from the adsorption branch of the isotherms are listed in Table 1. It was observed that when the plain THS sample underwent calcination, the surface area was

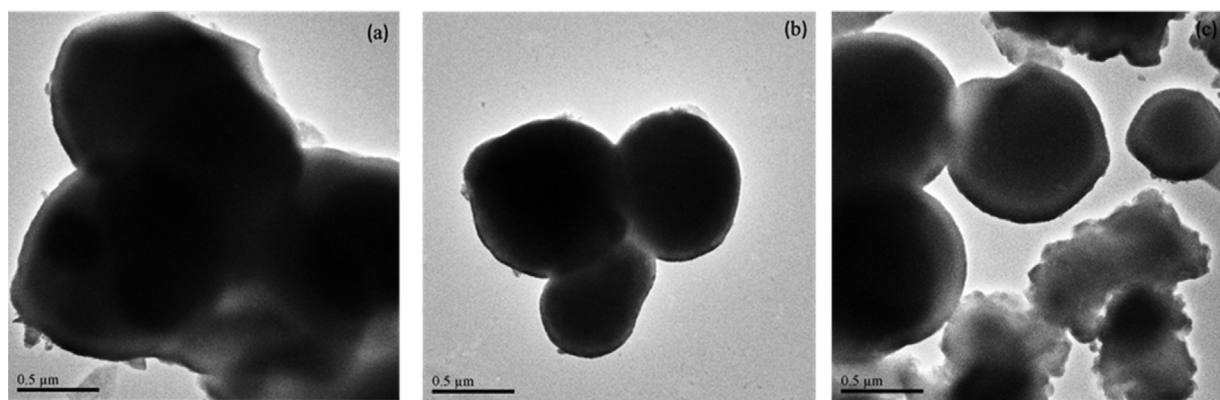
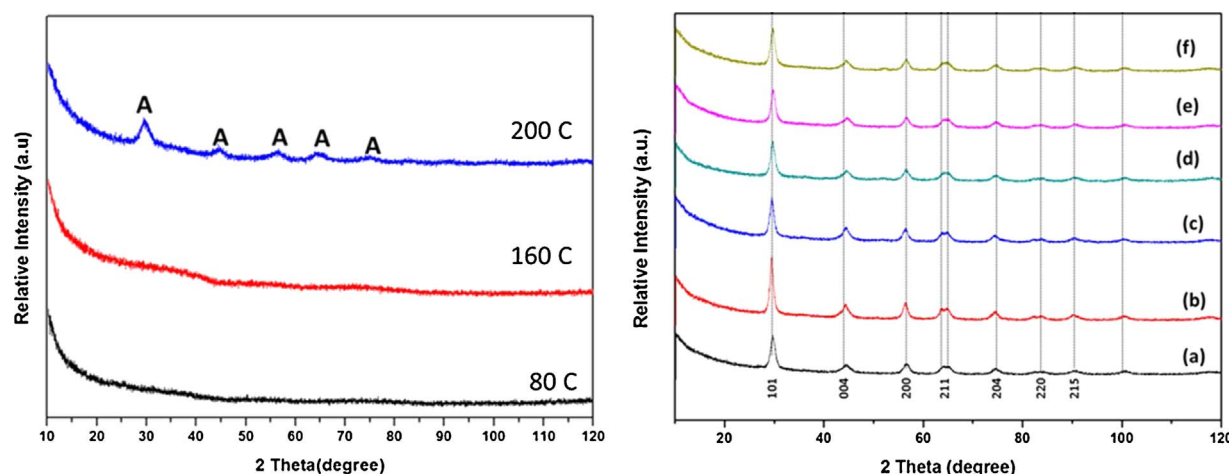


Fig. 5. TEM Images of THS prepared from Ti/ethanol ratio of 1:10, and refluxed at varying temperatures: (a) 80 °C, (b) 160 °C, 200 °C.



**Fig. 6.** XRD patterns of THS subjected to varying hydrothermal treatment temperatures (left); XRD Patterns of prepared metal impregnated Anatase THS calcined in  $\text{H}_2/\text{N}_2$  at 450 °C for 3 h, (a) THS@450 °C, (b) Cu/THS, (c) Ag/THS, (d) Co/THS, (e) Cr/THS, (f) Ni/THS (right).

reduced from 156 to 122  $\text{m}^2/\text{g}$  and the average pore diameter increased from 21,476 to 43,702 Å. For the metal impregnated samples, the surface areas decreased to the range of 75–97  $\text{m}^2/\text{g}$ , with pore diameters of 3.44–3.87 nm, respectively. This decrease was attributed to the metal loaded blocking the pores of the  $\text{TiO}_2$  [33].

### 3.5. UV-vis DRS

Fig. 8 depicts the diffusion reflectance spectra of the plain THS, calcined THS, as well as metal-impregnated THS. It was observed from the spectra that the plain THS displayed an absorption edge of approximately 380 nm which corresponds to a band gap energy of 3.2 eV [34], which suggests that these plain THS can absorb only UV light. A further observation was that by annealing the THS in hydrogen, the absorption range of the THS was effectively shifted into the visible light region of 400–500 nm; the absorption edge of the THS annealed/calcined in hydrogen was estimated to be 475 nm. This red shift to the visible light region is attributed to the unique nanostructured particles with mesoporous shells which serve as a path for light transfer, permitting the light to penetrate the photocatalyst deeply [35], and to the hollow chambers into which the incident photon light in flux is introduced, thereby generating multiple light reflections and scattering; which, in turn, promotes light harvesting and enhancement of the light-activated surface area [36–38].

A small red shift into the visible light absorption region at about 415–430 nm was observed for the metal-impregnated THS samples (Table 1), which was attributed to the metals loaded on the surface of the THS samples. Furthermore, the metals impregnation on the THS formed the impurity level between the conduction band and valence band, narrowing the band gap [39]. The band gap energies ( $E_g$ ) of the prepared samples were estimated from the UV-vis spectra by Tauc plot of  $(ahv)^2$  vs  $(hv)$  and extrapolation of the linear portions of the curves to the energy axis according to [40,34,41] (Fig. 9):

$$ahv = B (hv - E_g)^{1/2} \quad (1)$$

Where  $\alpha$  is the absorption coefficient,  $hv$  is the photon energy,  $E_g$  is the direct energy, and  $B$  is a constant. The absorption coefficient ( $\alpha$ ) was determined from the relation  $A = I/I_0 = e^{(-\alpha d)}$ , or it can be calculated using the well-known relation deduced from Beer-Lambert's relation,  $\alpha = 2.303A/d$ , where  $d$  is the path length of the quartz cuvette and  $A$  is the absorbance determined from the UV-vis spectrum [42]. The Tauc plots of the plain and metal impregnated THS are depicted in Fig. 10. The estimated band gap energies (Table 1) from the Tauc plots shows that impregnating THS with transition metals narrows the THS band gap; and therefore facilitates the absorption of visible light [34].

Scheme 2 illustrates the CB and VB edge potential of the TH samples (Table 1), which were calculated using the Mulliken electronegativity theory [43]:

$$E_{VB} = X - E_E + 0.5E_g \quad (2)$$

Where  $E_{VB}$  is the VB edge potential,  $X$  is the electronegativity of the semiconductor, which is the geometric mean of the electronegativity of the constituent atoms (EN of  $\text{TiO}_2$  is 5.81 eV);  $E_g$  is the band gap. The CB edge potential can subsequently be calculated from:

$$E_{CB} = E_{VB} - E_g \quad (3)$$

It can be observed from Scheme 1 how the band gap energy of the THS is decreased once impregnated with transition metals, in order to facilitate the photoreforming of glycerol and subsequent reduction of  $\text{H}^+$  into  $\text{H}_2$ .

### 3.6. Photoluminescence studies

The PL spectroscopy was utilized to study the recombination of the photo-induced electron-hole pairs generated and the charge trapping efficiencies of the prepared semiconductor samples. The best excitation wavelengths of the prepared samples were determined from the

**Table 1**

Specific surface area, pore structure parameters, and band gap energies of the prepared samples.

Samples	$S_{BET}$ ( $\text{m}^2/\text{g}$ )	Pore Volume ( $\text{cm}^3/\text{g}$ )	Pore Diameter (Å)	Crystallite size (nm)	Band gap (eV)	CB Potential (eV)	VB Potential (eV)	$\lambda_{ex}$ (nm)
Plain THS	155	0.081	21.5	3.9	3.2	-0.29	2.91	-
THS@450C	122	0.133	43.7	20	2.26	0.18	2.44	350
Ag/THS	75.8	0.067	35.3	11.5	2.4	0.11	2.51	375
Co/THS	90.3	0.081	36.2	10.6	2.8	-0.09	2.71	382
Cr/THS	96.8	0.083	34.4	10.6	2.35	0.135	2.485	380
Cu/THS	80.6	0.058	38.7	13.5	2.25	0.185	2.435	382
Ni/THS	86.6	0.077	35.8	10.9	2.8	-0.09	2.71	378

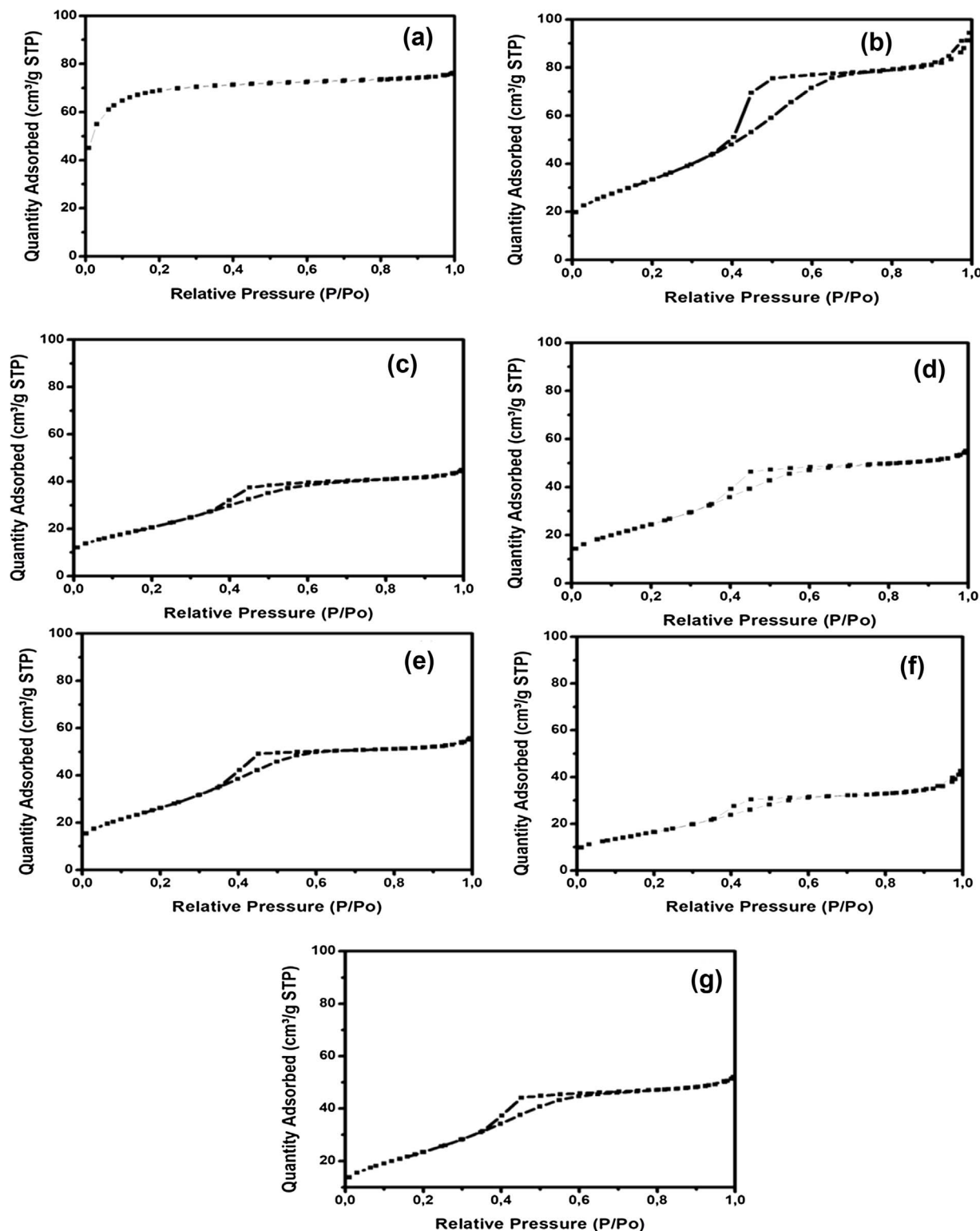


**Fig. 7.** Nitrogen adsorption-desorption isotherms of: (a) plain THS, (b) THS@450 °C, (c) Ag/THS, (d) Co/THS, (e) Cr/THS, (f) Cu/THS, (g) Ni/THS. All impregnated samples were calcined in H<sub>2</sub>/N<sub>2</sub> at 450 °C for 3 h.

photoluminescence excitation studies. Fig. 11(a) shows the PL excitation spectra of the prepared materials recorded with an emission of 500 nm. The excitation wavelengths of the materials were ascribed to the peaks with sharp intensities; which suggested that the excitation wavelengths ( $\lambda_{\text{ex}}$ ) of the prepared samples were within the range of 350–385 nm (Table 1); and attributed to the emission of band gap transition with the energy of light approximately equal to the band gap

energy (387.5 nm) of anatase [44,45]. Fig. 11(b) depicts the PL emission spectra of the prepared samples recorded using their best excitation wavelengths. It is observed that the most intense peak of the PL emissions for all samples was recorded at 430 nm, due to the band-band PL phenomenon [45]. Furthermore, it was observed that the intensity of the peaks of the samples decreased in the order Cr/THS < Co/THS < Ag/THS < Cu/THS < Ni/THS < THS. This decrease in the

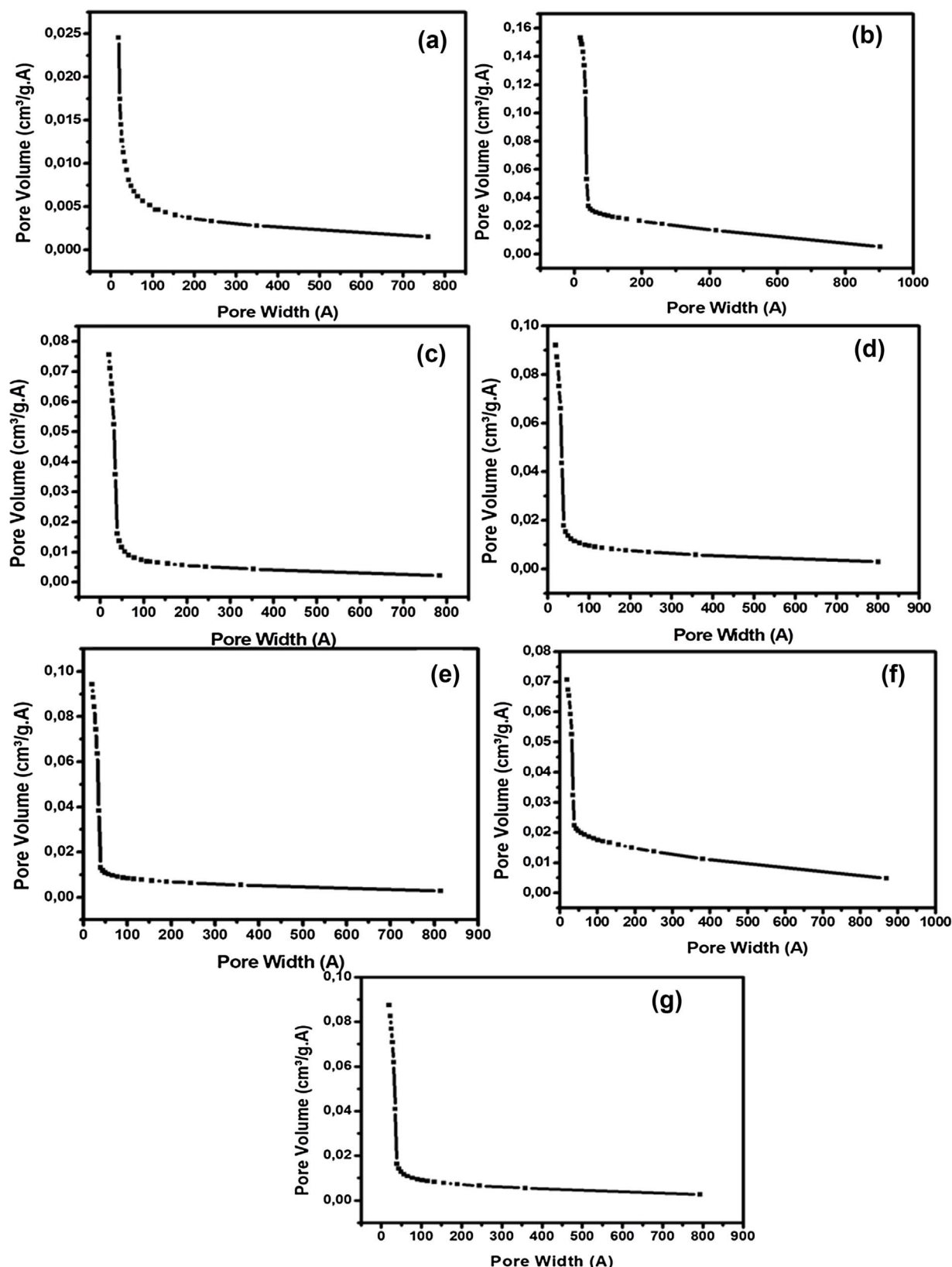


**Fig. 8.** BJH pore size distribution plot of: (a) plain THS, (b) THS@450 °C, (c) Ag/THS, (d) Co/THS, (e) Cr/THS, (f) Cu/THS, (g) Ni/THS. All impregnated samples were calcined in H<sub>2</sub>/N<sub>2</sub> at 450 °C for 3 h.

PL peak intensity is attributed to the movement of the photoexcited electrons from the THS conduction band to the metals centres, thereby inhibiting the electron-hole pair recombination; which results in an increase in photocatalytic activity [46–48].

#### 4. Photocatalytic H<sub>2</sub> production and mechanism

The photocatalytic performance of the prepared catalysts for production of hydrogen via simultaneous glycerol reforming and water

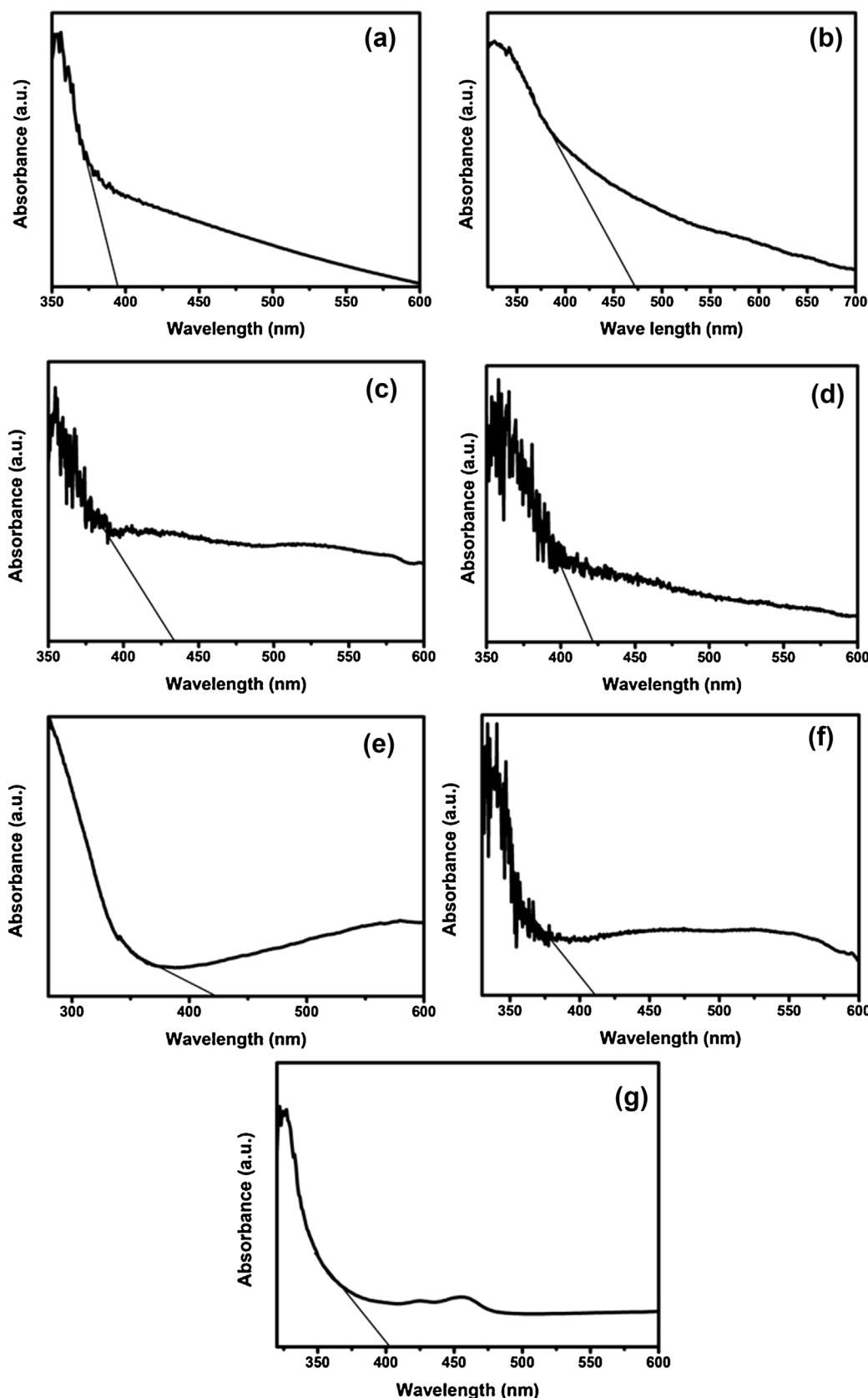


**Fig. 9.** DRS Analysis of, (a) plain THS, (b) THS-450 annealed in  $\text{H}_2/\text{N}_2$  at  $450\text{ }^\circ\text{C}$ , (c) Cu/THS, (d) Ni/THS, (e) Ag/THS, (f) Cr/THS, (g) Co/THS.

splitting process were tested under solar irradiation conditions. Fig. 12 shows the rates of hydrogen production using the prepared catalysts. It was observed that during the first hour of the experiment, no hydrogen was produced when THS@450 was utilized as a photocatalyst;

however, at the end of the 4 h experiment,  $693.9\text{ }\mu\text{mol h}^{-1}\text{ g}^{-1}$  of hydrogen was produced by the THS@450 sample; which was two to five times greater than the previously reported by several authors [20,49]. Several authors have reported on the role of THS for the improvement

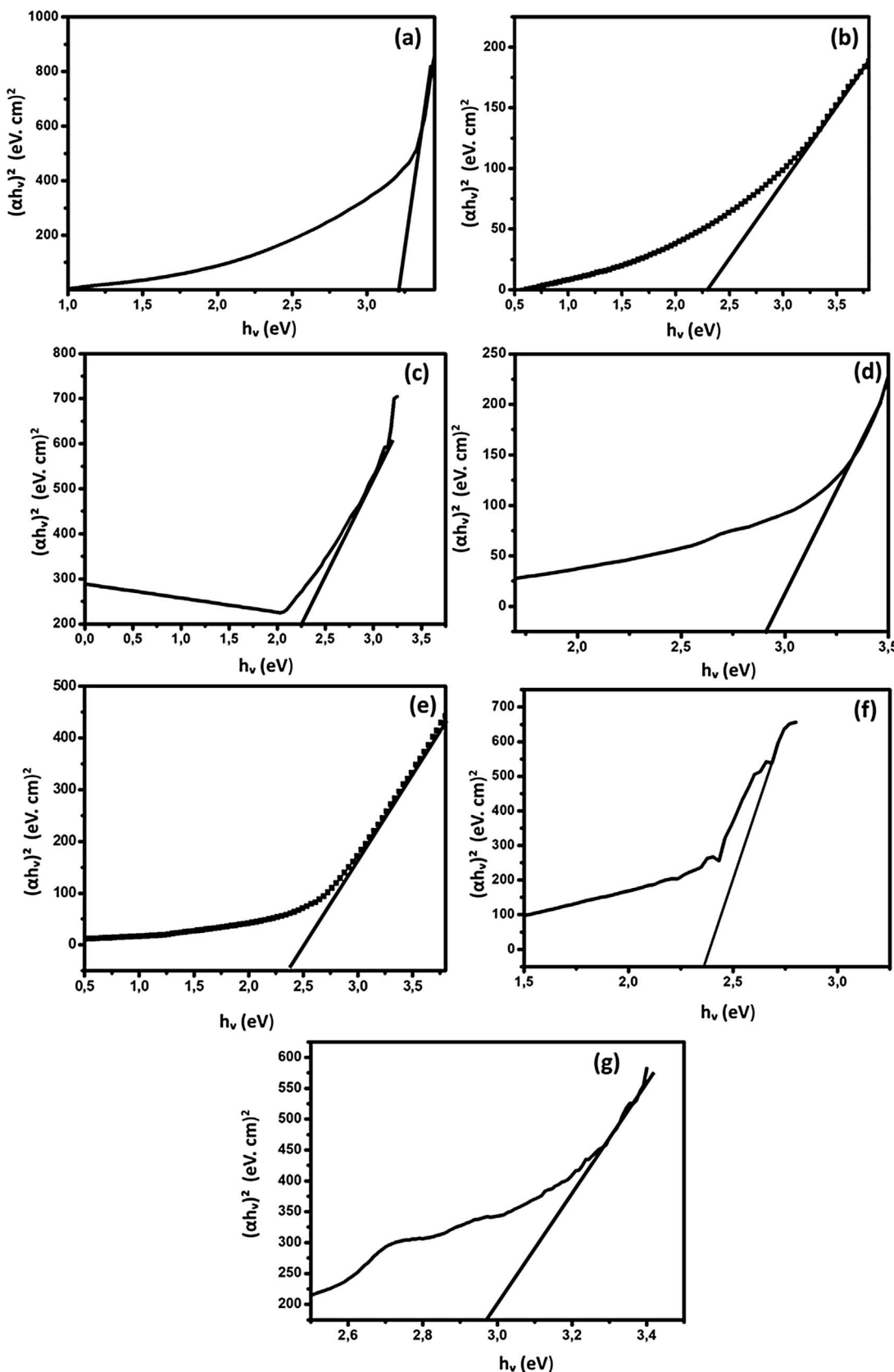
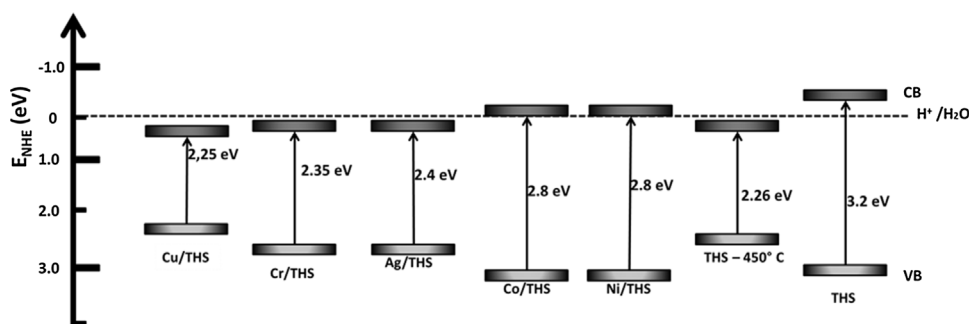


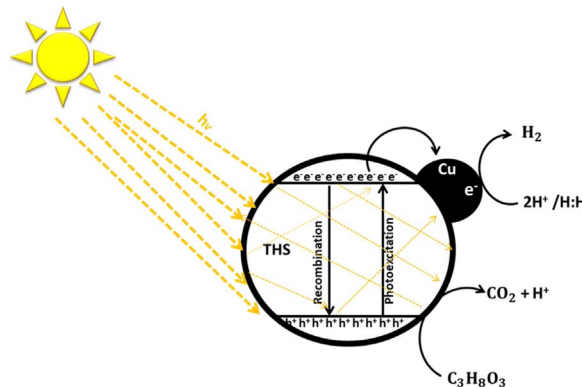
Fig. 10. Tauc plots of, (a) plain THS, (b) THS-450 annealed in  $\text{H}_2/\text{N}_2$  at  $450^\circ\text{C}$ , (c) Cu/THS, (d) Ni/THS, (e) Ag/THS, (f) Cr/THS, (g) Co/THS.

of photocatalytic activity. The enhanced activity of the THS during the  $\text{H}_2$  evolution is attributed to the large surface area that traps more sacrificial glycerol molecules onto its active site, and facilitate

simultaneous water splitting and glycerol oxidation. In addition, the harvesting of visible light (due to the narrowed band gap of  $2.62\text{ eV}$ ) and creation of multiple reflections inside the hollow chambers, leads to



**Scheme 1.** Energy band diagram of plain THS, THS@450 °C and M/THS photocatalysts.



**Scheme 2.** Illustration of the solar photocatalytic hydrogen production mechanism from glycerol reforming, over Cu/THS photocatalyst.

increased rate of photoinduced electron/hole pair generation and concomitant lower rates of recombination [50–52,48,53,54,23,55].

It was observed that the incorporation of some of the transition metals on the surface of the THS improved the solar photocatalytic hydrogen production activity. The enhanced activity of the M/THS (metal impregnated THS) followed the order of Cu/THS ( $16775 \mu\text{mol h}^{-1} \text{g}^{-1}$ ) > Ag/THS ( $6370 \mu\text{mol h}^{-1} \text{g}^{-1}$ ) > Ni/THS ( $1473 \mu\text{mol h}^{-1} \text{g}^{-1}$ ) > Co/THS ( $1859 \mu\text{mol h}^{-1} \text{g}^{-1}$ ) > Cr/THS ( $594 \mu\text{mol h}^{-1} \text{g}^{-1}$ ). It is suggested that the main factors that play a crucial role in the activity of the photocatalyst are, structure, morphology, light harvesting, and electron/hole mobilization and separation [56].

This enhanced activity is supported by the UV-vis DRS analysis which confirmed that the incorporation of the transition metals to the surface of the anatase THS can effectively reduce the band gap energy,

which in turn promotes the solar harvesting and improvement in photoinduced surface area, thereby enhancing the generation of photoinduced electron/hole pairs [57]. The PL analysis also showed that the loading of transition metal leads to the prevention of the photoinduced electron/pair recombination. The low activity of Ni/THS photocatalyst can be attributed to the high electron/hole pair recombination efficiency, which is supported by the PL analysis; as it was observed that the Ni/THS catalyst exhibited relatively similar electron/hole recombination efficiency to that of THS@450. This finding implies that the impregnation of the THS with Ni resulted in the narrowing of the band gap, but with little effect on the reduction of the electron/hole recombination efficiency, as observed from the PL analysis.

From the PL analysis, it was expected that the Cr/THS, which shows the highest prevention of electron/hole pair recombination, would produce the highest quantity of hydrogen. In fact, the Cr/THS produced the lowest hydrogen quantity. This might be attributed to the bright color of Cr when immersed in water, which might have led to light scattering that prevented some of the solar irradiation striking the surface of the THS for electron excitation, which in turn lead to poor generation of photoinduced electron/hole pairs [58]. Larsen et al., [59] attributed this loss of activity to the formation of surface and intergranular Cr(IV) oxide clusters, which act as recombination centres and reside over the catalytically active sites on the TiO<sub>2</sub> surface.

The Co/THS, Ag/THS, and Cu/THS catalysts shared relatively similar electron/hole pair recombination efficiencies, but the Cu/THS outperformed the two catalysts during the hydrogen production experiments (Fig. 12). The excellent activity of the Cu/THS was attributed to the synergy between Cu ions and the THS particles which was confirmed by the XRD analysis as well as the DRS analysis. During the impregnation and calcination steps, it was observed that the incorporation of Cu ions on to the crystal lattice of the THS did not greatly reduce the crystallinity of the THS, compared to the situation with the use of other transition metals. This suggests that the Cu/THS sample

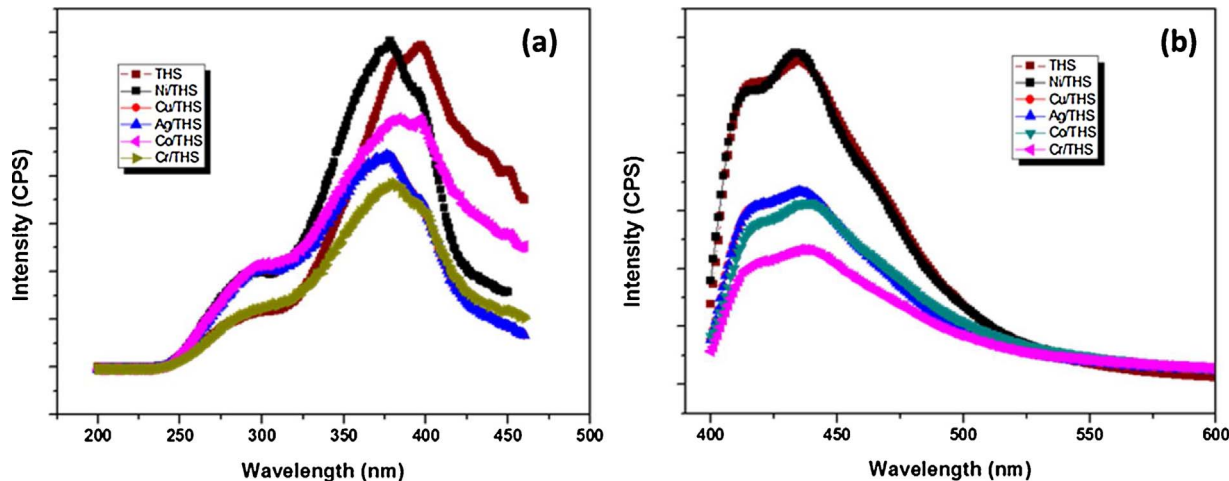


**Fig. 11.** Photoluminescence spectra of the prepared samples: (a) Excitation Spectra and (b) Emission Spectra.

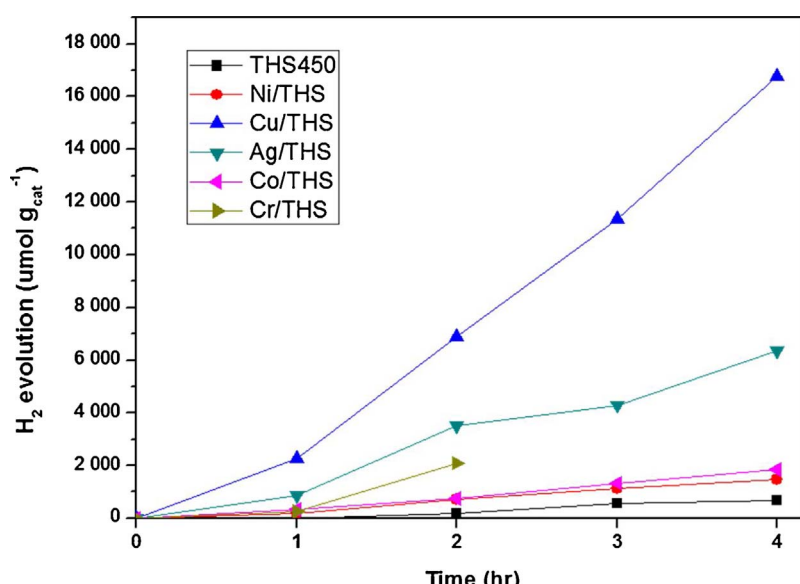


**Fig. 12.** Solar hydrogen production activity of various prepared catalysts: reaction mixture: 5% (v/v) glycerol:water, catalyst: 100 mg.

contained more active anatase crystallite sites, which resulted in excellent activity during the photocatalytic production of hydrogen [60–62]. Furthermore, the DRS analysis and the Tauc plots showed that the Cu/THS sample had the lowest band gap energy, which might have resulted in the highest photoinduced electron/hole generation. Moreover, the fast reduction of Cu<sup>+</sup> to Cu<sup>0</sup> enhances the activity of the Cu/THS and subsequently accelerates the rate of H<sub>2</sub> recombination [63]; due to its recombination rate constant which is higher than that of Cu<sub>2</sub>O and even higher than that of Au [64].

Yang et al., [65], prepared Co/TiO<sub>2</sub> catalyst for hydrogen production. During the first four hours of their experiment their Co/TiO<sub>2</sub> evolved no hydrogen. However, they discovered that hydrogen was produced during the first four hours of the experiments, and the reason that it was not detected during the GC analysis was because it was stored on the Co active layer of the catalyst, from the TG analysis. Furthermore, during that first four hours of the experiment, the hydrogen storage capacity of Co reached capacity; and after reaching saturation, hydrogen evolution was observed. Therefore, they proposed that the Co/TiO<sub>2</sub> catalysts can produce and store hydrogen, and this proposal opens new doors for the development of photocatalysts for simultaneous production and storage of hydrogen. An investigation of this specific aspect was, however, beyond the scope of this work.

A plausible mechanism for the hydrogen evolution from the photocatalytic reforming of glycerol over plain THS and M/THS photocatalyst is depicted in Scheme 2, which can be described in the following equation:



During the photoexcitation of the plain THS, the VB electrons (e<sup>-</sup>) migrate to the CB, generating holes (h<sup>+</sup>) in the VB. The generated electron/hole pair of the THS was found to have a high rate of recombination from the PL analysis, and therefore only a fraction of the pair take part on the glycerol photocatalytic reforming process, resulting in low photocatalytic hydrogen evolution activity [66,67]. However, when the THS were impregnated with transition metals nanoparticles (M), the electrons from the CB of the THS migrate to the M, resulting in the equilibration of fermi level (9.9.5 eV) of THS which higher than the fermi level of Cu (7.1 eV) and the creation of the Schottky barrier at the interface [68–71]. The Schottku barrier is responsible for the migration of the generated VB electrons from the THS to the surface of transition M, and these electrons are subsequently involved in the reduction of protons (H<sup>+</sup>) to produce H<sub>2</sub>. Furthermore, the photo-induced holes (h<sup>+</sup>) trapped on the surface of the THS are

scavenged by glycerol present in the reaction process, which in turn generates H<sup>+</sup> that subsequently undergo reduction with photo-excited electrons to form H<sub>2</sub> [63,72,73].

## 5. Conclusions

In summary, the THS hollow spheres were successfully prepared via a facile hydrothermal method. The ratio of titania to ethanol plays a crucial role in the formation of the hollow spherical particles. The incorporation of transition metals on the THS surface does not only reduce the band gap energy of the material for visible light harvesting, but also slows down the rate of electron/hole recombination, thereby increasing the photocatalytic activity. The Cu/THS catalyst exhibited the highest activity for hydrogen production from glycerol solar photocatalytic reforming.

## Acknowledgements

We are grateful for the generous financial support of this work from Mintek, South Africa and the University of South Africa (Research Flagship CREATE (Catalytic Reaction Technology and the Transformation of Energy), and the South African National Research Foundation (NRF).

## References

- [1] M. Rahman, M. Khan, M. Ullah, X. Zhang, A. Kumar, A hybrid renewable energy system for a north off-Grid community, *Energy* 97 (2016) 151–160.
- [2] M. Pretoriusse, L. Valverde, D. Cocco, G. Cau, J. Guerra, Real-time intergration of optimal generation scheduling with MPC for the energy management of a renewable-based hydrogen-based microgrid, *Appl. Energ.* 166 (2016) 96–106.
- [3] B. Shafiei, B. Davidsdottir, J. Leaver, H. Stefansson, E. Asgeirsson, Comparative analysis of hydrogen, biofuels and electrical transitional pathways to sustainable transporting the renewable-based energy system, *Energy* 183 (2015) 614–627.
- [4] H. Kim, S. Lee, A. Upadhye, I. Ro, M. Tejedor, M. Anderson, W. Kim, G. Huber, Plasmon-enhanced photoelectrochemical water splitting with size-controllable gold nanodots arrays, *ACS Nano* 8 (2014) 10756–10765.
- [5] C. Gai, Y. Guo, T. Liu, N. Peng, Z. Liu, Hydrogen-rich gas production by steam gasification of hydrochar derived from sewage sludge, *Int. J. Hydrogen Energy* 41 (2016) 3363–3372.
- [6] J. Remon, F. Broust, J. Valette, Y. Chhiti, I. Alava, A. Fernandez-Akarregi, Production of a hydrogen-rich gas from the fast pyrolysis bio-oils: comparison between homogeneous and catalytic steam reforming routes, *Int. J. Hydrogen Energy* 39 (2014) 171–182.
- [7] O. James, S. Maity, M. Mesubi, K. Ogunniran, T. Siyanbola, E. Sahu, Towards reforming technologies for production of hydrogen exclusively from renewable resources, *Green Chem.* 13 (2011) 2272–2284.
- [8] X. Li, J. Yu, J. Low, Y. Fang, J. Xiao, X. Chen, Engineering heterogeneous

semiconductors for solar water splitting, *J. Mater. Chem. A* 3 (2015) 2485–2534.

[9] H. Bahruji, M. Bowker, P. Davies, L. Al-Mozroai, A. Dickson, J. Greaves, D. James, L. Millard, F. Pedrono, Sustainable H<sub>2</sub> gas production by photocatalysis, *J. Photochem. Photobiol. A: Chem.* 2–3 (2010) 115–118.

[10] S. Song, Y. Zhang, Y. Xing, C. Wang, J. Feng, W. Shi, W. Zheng, H. Zhang, Rectangular AgIn(WO<sub>4</sub>)<sub>2</sub> nanotubes: a promising photoelectric material, *Adv. Funct. Mater.* 18 (16) (2008) 2328–2334.

[11] Y. Li, R. Jin, Y. Xing, J. Song, X. Liu, M. Li, R. Jin, Macroscopic foam-like holey ultrathin g-C<sub>3</sub>N<sub>4</sub> nanosheets for drastic improvement of visible-light photocatalytic activity, *Adv. Energy Mater.* 6 (24) (2016) 1601273.

[12] T. Jafari, E. Moharreri, A.S. Amin, R. Miao, W. Song, S. Suib, Photocatalytic water splitting – The untamed dream: a review of recent advances, *Molecules* 21 (7) (2016) 900–928.

[13] X. Zou, Y. Zhang, Noble free metal-free hydrogen evolution catalysts for water splitting, *Chem. Soc. Rev.* 44 (2015) 4180–5148.

[14] M. Gholipour, C. Dihm, F. Beland, T. Do, Nanocomposition heterojunctions as sunlight-driven photocatalyst for hydrogen production from water splitting, *Nanoscale* 7 (18) (2015) 8187–8208.

[15] Z. Sun, T. Liao, J. Kim, K. Liu, L. Jiang, J. Kim, Architecture designed ZnO hollow microspheres with wide-range visible light photoresponses, *J. Mater. Chem. C* 1 (2013) 6924–6929.

[16] J. Xu, W. Dai, J. Li, Y. Cao, H. Li, K. Fan, Novel core-shell structured mesoporous titania microspheres: preparation characterization and excellent photocatalytic activity in phenol abatement, *J. Photochem. Photobiol. A: Chem.* 195 (2) (2008) 284–294.

[17] T. Nakashima, N. Kimizuka, Interfacial synthesis of hollow TiO<sub>2</sub> microspheres in ionic liquids, *J. Am. Chem. Soc.* 125 (21) (2003) 6386–6387.

[18] H. Strohm, P. Lobmaan, Porous TiO<sub>2</sub> hollow spheres by liquid phase deposition on polystyrene latex-stabilised pickering emulsion, *J. Mater. Chem.* 14 (17) (2004) 2267–2273.

[19] R. Liu, H. Yoshida, S. Fujita, M. Arai, Photocatalytic hydrogen production from glycerol and water with NiOx/TiO<sub>2</sub>, *Appl. Catal. B: Environ.* 144 (2014) 41–45.

[20] B. Wang, X.-Y. Lu, L. Yu, J. Xuan, M. Leung, H. Guo, Facile synthesis of TiO<sub>2</sub> hollow spheres composed of high percentage of reactive facets for enhanced photocatalytic activity, *CrystEngComm* 16 (2014) 10046–10055.

[21] B. Lei, P. Zhang, H. Qiao, X. Zheng, Y. Hu, G. Huang, Z. Sun, X. Zhang, A facile template-free route for synthesis of anatase TiO<sub>2</sub> hollow spheres for dye-sensitized solar cells, *Electrochim. Acta* 143 (2014) 129–134.

[22] R. Liu, F. Ren, J. Yang, W. Su, Z. Sun, L. Zhang, C. Wang, One-step synthesis of hierarchically porous hybrid TiO<sub>2</sub> hollow spheres with high photocatalytic activity, *Front. Mater. Sci.* 10 (2016) 15–22.

[23] J. Yu, S. Liu, H. Yu, Microstructures and photoactivity of mesoporous anatase hollow microspheres fabricated by fluoride-mediated self transformation, *J. Catal.* 249 (2007) 59–66.

[24] J. Li, J. Xu, W. Dai, H. Li, K. Fan, Direct hydro-alcohol thermal synthesis of special core-shell structured Fe-doped titania microspheres with extended visible light response enhanced, *Appl. Catal. B: Environ.* (2007) 162–170.

[25] Y. Zhao, F. Pan, H. Li, D. Zhao, L. Liu, Q. Xu, W. Chen, Uniform mesoporous anatase-brookite biphase TiO<sub>2</sub> hollow spheres with high crystallinity via oswald ripening, *J. Phys. Chem. C* 117 (2013) 21718–21723.

[26] H. Klong, L. Alexander, X-Ray Diffraction Procedures for Crystalline and Amorphous Solids, Wiley, New York, 1954.

[27] H. Guo, D. Tian, L. Liu, Y. Wang, Y. Guo, X. Yang, Core-shell TiO<sub>2</sub> microspheres with enhanced photocatalytic activity and improved lithium storage, *J. Solid State Chem.* 201 (2013) 137–143.

[28] D. Kim, S. Kwak, Hydrothermal synthesis of mesoporous TiO<sub>2</sub> with high crystallinity, thermal stability, large surface area, and enhanced photocatalytic activity, *Appl. Catal. A: Gen.* 323 (2007) 110–118.

[29] J. Yu, T. Ma, S. Liu, Enhanced photocatalytic activity of mesoporous TiO<sub>2</sub> aggregates by embedding carbon nanotubes as electron, *Phys. Chem. Chem. Phys.* 13 (8) (2000) 3491–3501.

[30] H. Zaid, C. Kait, M. Mutalib, Preparation and characterization of Cu-Fe/TiO<sub>2</sub> photocatalyst for visible light deep desulfurization, *Malaysian J. Anal. Sci.* 20 (4) (2016) 713–725.

[31] A. Kim, M. Kang, Effect of Al-Cu bimetallic components in a TiO<sub>2</sub> framework for high hydrogen production TiO<sub>2</sub> photocatalyst for hydrogen production on methanol/water photo-splitting, *Int. J. Photoenergy* (2012) 1–9.

[32] S. Obregon, S. Lee, V. Rodriguez-Gonzalez, Loading effects of silver on hydrogen photoproduction using a Cu-TiO<sub>2</sub> photocatalyst, *Mater. Lett.* 173 (2016) 174–177.

[33] J. Reddy, K. Lalitha, P. Reddy, G. Sadanandam, M. Subrahmanyam, V. Kumari, Fe/TiO<sub>2</sub>: A visible light active photocatalyst for the continuous production of hydrogen from the water splitting under solar irradiation, *Catal. Lett.* 144 (2014) 340–346.

[34] G. Jeong, J.-G. Kim, M.-S. Park, M. Seo, S. Hwang, Y.-U. Kim, Y.-J. Kim, J. Kim, S. Dou, Core-shell structured silicon nanoparticles@TiO<sub>2-x</sub>/Carbon mesoporous microfiber composite as a safe and high-performance lithium-ion battery anode, *ACS Nano* 8 (3) (2014) 2895–2977.

[35] B. Fang, Y. Xing, A. Bonakdarpour, S. Zhang, D. Wilkinson, Hierarchical CuO-TiO<sub>2</sub> hollow microspheres for highly efficient photodriven reduction of CO<sub>2</sub> to CH<sub>4</sub>, *ACS Sustain. Chem. Eng.* 3 (10) (2015) 2381–2388.

[36] B. Fang, A. Bonakdarpour, K. Reilly, Y. Xing, F. Taghipour, D. Wilkison, Large-scale synthesis of TiO<sub>2</sub> microspheres with hierarchical nanostructure for highly efficient photodriven reduction of CO<sub>2</sub> to CH<sub>4</sub>, *ACS Appl. Mater. Interfaces* 6 (2014) 15488–15498.

[37] B. Liu, K. Nakata, M. Saito, H. Saito, T. Ochiai, T. Murakami, K. Takagi, A. Fujishima, Hierarchical TiO<sub>2</sub> spherical nanostructures with tunable pore size, pore volume, and specific area: facile preparation and high photocatalytic performance, *Catal. Sci. Technol.* 2 (2012) 1933–1939.

[38] X. Wang, J. Yu, C. Ho, Y. Hou, X. Fu, Photocatalytic activity of a hierarchically macro/mesoporous titania, *Langmuir* 3 (2005) 3670–3678.

[39] X. Wang, S. Zhu, Y. Liang, Z. Cui, X. Yang, C. Liang, A. Inoue, Synthesis of Br-doped TiO<sub>2</sub> hollow spheres with enhanced photocatalytic activity, *J. Nanopart. Res.* 19 (2) (2017) 72.

[40] N. Soltani, E. Siaon, M. Hussein, M. Erfani, A. Abedini, G. Bahmanrokh, M. Navasery, P. Vaziri, Visible light-induced degradation of methylene blue in the presence of photocatalytic ZnS and CdS nanoparticles, *Int. J. Mol. Sci.* 13 (10) (2012) 12242–12258.

[41] Y. Li, L. Fang, R. Jin, Y. Yang, X. Fang, Y. Xing, S. Song, Preparation and enhanced visible light photocatalytic activity of novel g-C<sub>3</sub>N<sub>4</sub> nanosheets loaded with Ag<sub>2</sub>CO<sub>3</sub> nanoparticles, *Nanoscale* 7 (2) (2015) 758–764.

[42] J. Wu, Y. Zhao, N. Wang, Electrospinning of multilevel structured functional micro-/nanofibers and their applications, *J. Mater. Chem. A* 1 (25) (2013) 7290–7305.

[43] D. Kumar, V. Kumari, M. Karthik, M. Sathish, M. Shankar, Shape dependence structural, optical and photocatalytic properties of TiO<sub>2</sub> nanocrystals for enhanced hydrogen production via glycerol reforming, *Solar Energy Mater. Solar Cells* 163 (2017) 113–119.

[44] Q. Xiang, J. Yu, M. Jaroniec, Enhanced photocatalytic H<sub>2</sub>-production activity of grapheme-modified titania nanosheets, *Nanoscale* 3 (2011) 3670–3678.

[45] J. Yu, T. Ma, S. Liu, Enhanced photocatalytic activity of mesoporous TiO<sub>2</sub> aggregates by embedding carbon nanotubes as electron-transfer channel, *Phys. Chem. Chem. Phys.* 13 (8) (2011) 3491–3501.

[46] J. Liqiang, Q. Yichun, W. Baiqi, Review of photoluminescence performance of nanosized semiconductor materials and its relationship with photocatalytic activity, *Solar Energy Solar Cells* 90 (12) (2006) 1773–1787.

[47] S. Choi, S. Kim, S. Lim, H. Park, Photocatalytic comparison of TiO<sub>2</sub> nanoparticles and electrospun TiO<sub>2</sub> nanofibers: effect of mesoporosity and interparticle charge transfer, *J. Phys. Chem. C* 114 (39) (2010) 16475–16480.

[48] N. Murakami, Y. Kurihara, T. Tsubota, T. Ohno, Shape-controlled anatase titanium (IV) oxide particles prepared by hydrothermal treatment of peroxo titanic acid in the presence of polyvinyl alcohol, *J. Phys. Chem. C* 113 (8) (2009) 3062–3069.

[49] Q. Jiang, L. Li, J. Bi, S. Liang, M. Liu, Design and synthesis of TiO<sub>2</sub> hollow spheres with spatially separated dual cocatalyst for the efficient photocatalytic hydrogen production, *Nanomaterials* 7 (24) (2017).

[50] Q. Truong, T. Le, H. Hoa, Fluoride-free self-templated synthesis of hollow TiO<sub>2</sub> nanostructures for hydrogen evolution, *CrystEngComm* 14 (2012) 4274–4278.

[51] H. Zhou, T. Fan, J. Ding, D. Zhang, Q. Guo, Bacteria-directed construction of hollow TiO<sub>2</sub> micro/nanostructures with enhanced photocatalytic hydrogen evolution activity, *Opt. Express* 20 (102) (2012) 340–350.

[52] S. Liu, J. Yu, M. Jaroniec, Anatase TiO<sub>2</sub> with dominant high-energy {001} facets: synthesis, properties, and applications, *Chem. Mater.* 23 (18) (2011) 4085–4093.

[53] A. Selloni, Crystal growth:anatase shows its reactive side, *Nat. Mater.* 8 (2008) 614–627.

[54] H. Li, Z. Bian, J. Zhu, D. Zhang, G. Li, Y. Huo, H. Li, Y. Lu, Mesoporous titania spheres with tunable chamber structure and enhanced photocatalytic activity, *J. Am. Chem. Soc.* 129 (27) (2007) 8406–8407.

[55] Y. Jun, M. Casula, J. Sim, S. Kim, J. Cheon, A. Alivisatos, Surfactant-assisted elimination of a high energy facet as a means of controlling the shapes of TiO<sub>2</sub> nanocrystals, *J. Am. Chem. Soc.* 125 (51) (2003) 15981–15985.

[56] K. Dai, L. Lu, Q. Liu, G. Zhu, Q. Liu, Z. Liu, Graphene oxide capturing surface-fluorinated TiO<sub>2</sub> nanosheets for advanced photocatalysis and the reveal of synergism reinforce mechanism, *Dalton Trans.* 43 (5) (2014) 2202–2210.

[57] D. Lang, Q. Xiang, G. Qiu, X. Feng, F. Liu, Effects of crystalline phase and morphology on the visible light photocatalytic H<sub>2</sub> production activity of CdS nanocrystals, *Dalton Trans.* 43 (19) (2014) 7245–7253.

[58] X. Wang, S. Pehkonen, A. Ray, Removal of aqueous Cr (VI) by a combination of photocatalytic reduction and co-precipitation, *Indian Eng. Chem. Res.* 43 (7) (2004) 1665–1672.

[59] G. Larsen, R. Fitzmorris, J. Zhang, Y. Zhao, Structural, Optical, and Photocatalytic Properties of Cr: TiO<sub>2</sub> nanorod array fabricated by oblique and angle codeposition, *J. Phys. Chem. C* 115 (34) (2011) 16892–16903.

[60] V. Puddu, H. Choi, D. Ioniou, G. Puma, Photocatalysis for indoor air remediation: influence of crystallinity, crystal phase, and UV irradiation intensity on trichloroethylene degradation, *Appl. Catal. B: Environ.* 94 (1–3) (2010) 211–218.

[61] G. Chiarello, P. Di, L. Palmisano, E. Selli, Effects of titanium dioxide crystalline structure on the photocatalytic production of hydrogen, *Photochemical & Photobiol. Sci.* 10 (3) (2010) 355–360.

[62] M. Murdoch, G. Waterhouse, M. Nadeem, J. Metson, M. Keane, R. Howe, J. Llorca, H. Idriss, The effect of gold loading and particle size on photocatalytic hydrogen production from ethanol over Au/TiO<sub>2</sub> nanoparticles, *Nat. Chem.* 3 (6) (2011) 489–492.

[63] I. Majeed, M. Nadeem, A. Badshah, F.K. Kanodarwala, H. Ali, M. Khan, J. Stride, M. Nadeem, Titania supported MOF-199 derived Cu-Cu<sub>2</sub>O nanoparticles: highly efficient non-noble metal photocatalysts for hydrogen production from alcohol-mixtures, *Catal. Sci. Technol.* 7 (3) (2017) 677–686.

[64] L. Sinatra, A. LaGrow, W. Peng, A. Kirmani, A. Amassian, H. Idriss, O. Bakr, A Au/Cu<sub>2</sub>O-TiO<sub>2</sub> system for photocatalytic hydrogen production. A p-n-junction effect or a simple case of in situ reduction? *J. Catal.* 322 (1) (2015) 109–117.

[65] Y. Yang, P. Gao, Y. Wang, L. Sha, X. Ren, J. Zhang, P. Yang, T. Wu, Y. Chen, X. Li, A simple and efficient hydrogen production-storage hybrid system (Co/TiO<sub>2</sub>) for synchronized hydrogen photogeneration with uptake, *J. Mat. Chem. A* 5 (1) (2017) 9198–9203.

[66] J. Yu, J. Yu, W. Ho, Z. Jiang, L. Zhang, Effects of F-doping on the photocatalytic

activity and microstructures of nanocrystalline TiO<sub>2</sub> powders, *Chem. Mater.* 14 (9) (2002) 3808–3816.

[67] J. Yu, W. Wang, B. Cheng, B. Su, Enhancement of photocatalytic activity of mesoporous TiO<sub>2</sub> powders by hydrothermal surface fluorination treatment, *J. Phys. Chem. C* 113 (16) (2009) 6743–6750.

[68] H. Michaelson, The work function of the elements and its periodicity, *J. Appl. Phys.* 48 (11) (1977) 4729–4733.

[69] X. Wang, J. Yu, H. Yip, L. Wu, P. Wong, S. Lai, A mesoporous Pt/TiO<sub>2</sub> nanoarchitecture with catalytic and photocatalytic functions, *Chem. Eur. J.* 11 (10) (2005) 2997–3004.

[70] A.L. Linsebigler, G. Lu, J.T. Yates, Photocatalysis on TiO<sub>2</sub> surface: principles, mechanism, and selected results, *Chem. Rev.* 95 (3) (1995) 735–758.

[71] L. Gao, Y. Li, J. Ren, S. Wang, R. Wang, G. Fu, Y. Hu, Passivation of defect state in the anatase TiO<sub>2</sub> hollow spheres with Mg doping: realizing efficient photocatalytic overall water splitting, *Appl. Catal. B: Environ.* 202 (2017) 127–133.

[72] D. Kumar, M.L. Shankar, M. Kumari, G. Sadanandam, B. Srinivas, V. Durgakumari, Nano-size effects on CuO/TiO<sub>2</sub> catalysts for highly efficient H<sub>2</sub> production under solar irradiation, *Chem. Commun.* 49 (82) (2013) 9443–9445.

[73] Y. Yang, P. Gao, Y. Wang, L. Sha, X. Ren, J. Zhang, P. Yang, T. Wu, Y. Chen, X. Li, A simple and efficient hydrogen production-storage hybrid system (Co/TiO<sub>2</sub>) for synchronized hydrogen photogeneration with uptake, *J. Mater. Chem. A* 5 (2017) 9198–9203.